Multifunctionality in an Ion-Exchanged Porous Metal-Organic Framework

Sérgio M. F. Vilela,[a,b,*] Jorge A. R. Navarro,[c,*] Paula Barbosa,[d] Ricardo F. Mendes,[a] Germán Pérez-Sánchez,[a] Harriott Nowell,[e] Duarte Ananias,[a,f] Filipe Figueiredo,[d] José R. B. Gomes,[a] João P. C. Tomé,[g] Filipe A. Almeida Paz[a,*]

A contribution from

[a] *Department of Chemistry, CICECO – Aveiro Institute of Materials, University of Aveiro, 3810-193 Aveiro, Portugal*

[b] *Department of Chemistry,* LAQV-REQUIMTE*, University of Aveiro, 3810-193 Aveiro, Portugal*

[c] *Department of Inorganic Chemistry, University of Granada, 18071 Granada, Spain*

[d] *Department of Materials & Ceramic Engineering, CICECO – Aveiro Institute of Materials, University of Aveiro, 3810-193 Aveiro, Portugal*

[e] *Diamond Light Source, Didcot OX11 0DE, Oxon, Oxfordshire, United Kingdom*

[f] *Department of Physics, CICECO – Aveiro Institute of Materials, University of Aveiro, 3810-193 Aveiro, Portugal*

[g] *Departamento de Engenharia Química, Centro de Química Estrutural, Instituto Superior Técnico, Universidade de Lisboa, 1049-001 Lisboa, Portugal*

---

* *To whom correspondence should be addressed:*

Filipe A. Almeida Paz
Department of Chemistry, CICECO – Aveiro Institute of Materials
University of Aveiro
3810-193 Aveiro
Portugal

E-mail: filipe.paz@ua.pt
FAX: (+351) 234 401470
Telephone: (+351) 234 401418

Abstract

Porous robust materials are typically the primary selection of several industrial processes. Many of these compounds are, however, not robust enough to be used as multifunctional materials. This is typically the case of Metal-Organic Frameworks (MOFs) which rarely combine several different excellent functionalities into the same material. In this report we describe the simple acid-base post-synthetic modification of isotypical porous rare-earth-phosphonate MOFs into a truly multifunctional system, maintaining the original porosity features: [Ln(H_3pptd)]·*xSolvent* [where Ln^{3+} = Y^{3+} (**1**) and $(Y_{0.95}Eu_{0.05})^{3+}$ (**1_Eu**)] are converted into [K_3Ln(pptd)]·*zSolvent* [where Ln^{3+} = Y^{3+} (**1K**) and $(Y_{0.95}Eu_{0.05})^{3+}$ (**1K_Eu**)] by immersing the powder of **1** and **1K_Eu** into an ethanolic solution of KOH for 48 h. The K^+-exchanged Eu^{3+}-based material exhibits a considerable boost in CO_2 adsorption, being capable of being reused for several consecutive cycles. It can further separate C_2H_2 from CO_2 from a complex ternary gas mixture composed of CH_4, CO_2 and C_2H_2. This high adsorption selectivity is, additionally, observed for other gaseous mixtures, such as C_3H_6 and C_3H_8, with all these results being supported by detailed theoretical calculations. The incorporation of K^+ ions notably increases the electrical conductivity by four orders of magnitude in high relative humidity conditions. The conductivity is assumed to be predominantly protonic in nature, rendering this material as one of the best conducting MOFs reported to date.

1. Introduction

Metal-Organic Frameworks (MOFs) are a class of crystalline materials that have gained great interest in recent years, mainly due to their versatility and the ability to be used in a myriad of scientific areas. While MOFs have shown improvement over other materials in both materials chemistry and even biomedicine,[1] they further have great potential to overcome many of the limitations of other materials (such as zeolites, active carbons and ceramics) in diverse areas including gas storage and separation,[2-11] capture of hazardous chemicals,[12-16] heterogeneous catalysis,[17-20] for sensing,[21-26] drug delivery[27-30] and proton conductivity.[31-35] The presence of organic and inorganic components in MOFs paves the way to fine tune many of their properties (*e.g.*, porosity, luminescence and magnetism). Despite the known properties of MOFs, such as accessible channels, high thermal stability and existence of open metal sites, these materials still have room for more improvement by simple post-synthetic modifications (PSM). In fact, this versatility has gained particular interest in the last decade. While this has been more evident for gas adsorption/separation, in particular of CO_2, recent reports have described improvements of MOFs by PSM for fuel cell applications.[36] For years, MOFs have shown high CO_2 capture due to their large surface area and pore volumes. [37-39] Nevertheless, different approaches in MOF PSM have led to a boost in CO_2 uptakes, namely incorporation of cationic species[40-41] and amine pending groups.[42-45] While most PSM reported are directed to the organic component of MOFs, the more recent PSM approach of incorporating metallic cations instead of organic molecules showed remarkable improvement in different areas, such as photocatalysis[46-47] and ionic conductivity.[48] This ability to incorporate metallic cations is of particularly importance for energy-based devices. For example, the incorporation of lithium cations into the pores of MOFs have shown great results for the next-generation batteries.[49] Likewise, the incorporation of protons, usually associated to water, is also promising for application in fuel cells.[50-54]

Having this in mind, our research group has directed the attention to the potential application of Lanthanide-based MOFs (LnOFs) for both adsorption/separation processes and ionic conduction. We report herein a novel isotypical porous LnOF family of compounds, formulated as [Ln(H_3pptd)]·*x*Solvent [where Ln^{3+} = Y^{3+} (**1**) and $(Y_{0.95}Eu_{0.05})^{3+}$ (**1_Eu**) and solvent = water and/or methanol], resulting from the self-assembly of rare-earth/lanthanide cations with the tripodal and rigid organic linker (5'-(4-phenylphosphonic acid)-[1,1':3',1''-terphenyl]-4,4''-diyl)diphosphonic acid (**H_6pptd**). The properties of **1** were remarkably boosted by PSM through treatment with an ethanolic solution of KOH leading to the isolation of the ion-exchanged [K_3(Ln)(pptd)]·*z*Solvent [where Ln^{3+} = Y^{3+} (**1K**) and $(Y_{0.95}Eu_{0.05})^{3+}$ (**1K_Eu**), Solvent = water, methanol and/or ethanol] material. We note that the incorporation of K^+ considerably improves all the properties of the MOF:

- Gas sorption: while **1_Eu** could rapidly adsorb CO_2 into their pores, the adsorption capacity of **1K_Eu** towards CO_2 sequestration is considerably boosted, even at near ambient temperature (*i.e.*, 273 and 298 K), being scaled-up and reused for several consecutive cycles. **1K_Eu** is also

remarkably able to separate C_2H_2 from CO_2 in a complex ternary gas mixture composed of CH_4, CO_2 and C_2H_2.

- Ionic conduction: while **1_Eu** shows low conduction, reaching a maximum of 1.24×10^{-5} S cm^{-1} conductivity at 94 ºC and 98% relative humidity (RH), the incorporation of K^+ ions increased four orders of magnitude the conductivity reaching 0.189 S cm^{-1}, in the same conditions, being one of the highest conducting MOF materials reported to date. In fact, **1K_Eu** even presents a higher conductivity at 40 ºC and 20% RH than **1_Eu** at 94 ºC and 98% RH.

2. Results and Discussion

2.1. Design of the organic ligand and MOF preparation

The combination of phosphonate-based aromatic [*e.g.*, 1,4-phenylenebis(methylene)diphosphonic acid, (benzene-1,3,5-triyltris(methylene))triphosphonic acid and ((2,4,6-trifluorobenzene-1,3,5-triyl)tris(methylene))triphosphonic acid] or aliphatic [*e.g.*, nitrilotris(methylphosphonic acid) and (carboxymethyl)iminodi(methylphosphonic acid)] organic ligands have led in the past to different materials with 1D,[55] 2D[56-59] and dense 3D architectures.[60-61] The common structural feature resides in the presence of two or three methylene (-CH_2-) moieties, embodying the ligands with a high level of structural flexibility. We believe that this feature has hindered the isolation of highly porous 3D networks. To tackle this limitation, we employed the stiff large tripodal organic linker **H_6pptd** (synthesis and characterization in Figures S1 to S10 in the Supporting Information), previously used in the preparation of other MOFs.[62-66]

The self-assembly of this linker with Y^{3+} cations allowed the preparation of a porous 3D MOF, [Y(H_3pptd)]·*xSolvent* (**1**) (Scheme 1). Besides the standard hydro(solvo)thermal synthesis (Figure 1a), this MOF could be easily isolated by employing other synthetic approaches (more details in the Supporting Information) namely:

i) slow diffusion (at ambient temperature for several days);

ii) the *bench* "one-pot" approach (ambient temperature for 24 h);

iii) ionothermal synthesis (140 ºC for 72 h).

Compound **1** was stoichiometrically doped with 5% of Eu^{3+} (see Experimental Section in Supporting Information for further details). The resulting [($Y_{0.95}Eu_{0.05}$)(H_3pptd)]·*xSolvent* (**1_Eu**) material was characterized by using a set of standard solid-state techniques, with results suggesting that **1_Eu** shares the same crystalline phase with **1** (Figure 1b).

We emphasise that this MOF can be obtained at the gram scale by using the one-pot synthetic methodology under ambient conditions, an important feature concerning a competitive industrial production with low energy consumption. Nonetheless, the material can be prepared using various methods, in all cases as typically microcrystalline powders. We refer the reader to the Supporting Information which contains all the relevant structural characterization.

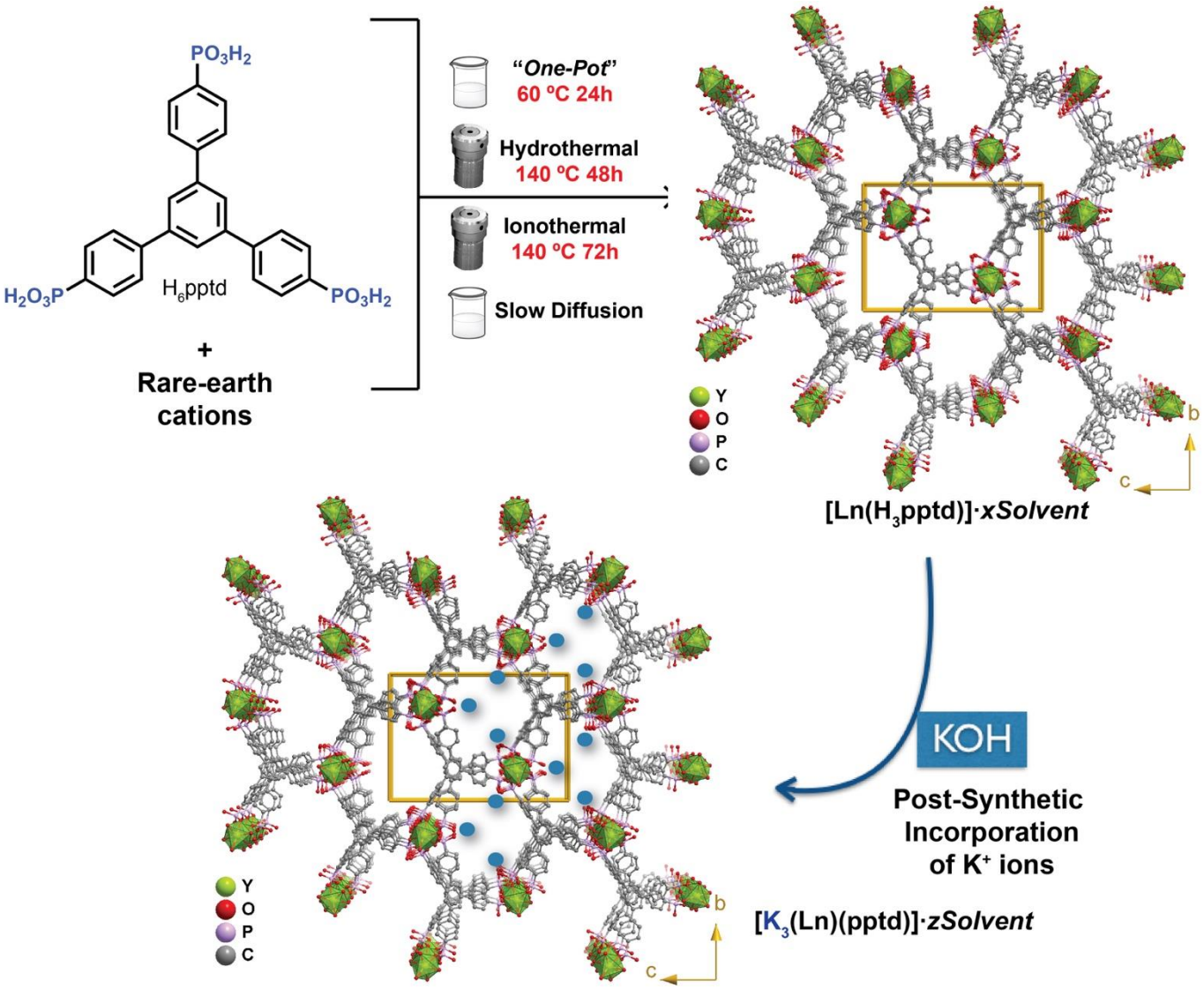

Scheme 1. Schematic representation of the preparation of **1** and **1_Eu** using four distinct experimental methods, and its post-synthetic modification by incorporating K^+ cations in the pores of the structure.

2.2. Structural Details

The structure of [Y(H_3pptd)]·*xSolvent* (**1**) could only be unveiled using synchrotron radiation from a microcrystal (several batches were tested typically giving the same unit cell parameters; the structural model is presented for the best collected data set). **1** crystallizes in the orthorhombic space group *P*na2_1, with the asymmetric unit being composed of a sole Y^{3+} metallic centre and one H_3pptd^{3-} organic linker (Figure S11 in the Supporting Information). The metallic centre has an unusual coordination sphere for LnOFs, {YO_6}, being hexacoordinated to six symmetry-related phosphonate groups, resembling an almost perfect octahedron. The H_3pptd^{3-} organic linker is connected to six symmetry-related metal centres in a simple κ^1 mode. This coordination mode leads to the formation of an inorganic chain along the [100] direction of the unit cell which, allied to the rigidity of the organic linker, promotes the formation of large pores along this direction (Figure 2).

These pores can be better viewed from a topological representation: Figure S12 (in the Supporting Information) depicts the reduction of the network to simple nodes (*i.e.*, the metal centers) and bridges (ensured by the organic linkers). Following the recommendations of Alexandrov *et al.*,[67] who suggested that any moiety (ligand or atoms) connecting more than two metallic centers should be considered as a network node, **1** is a simple unimodal 6-connected network with total point symbol $\{4^9.6^6\}$, as revealed by the software package TOPOS.[68]

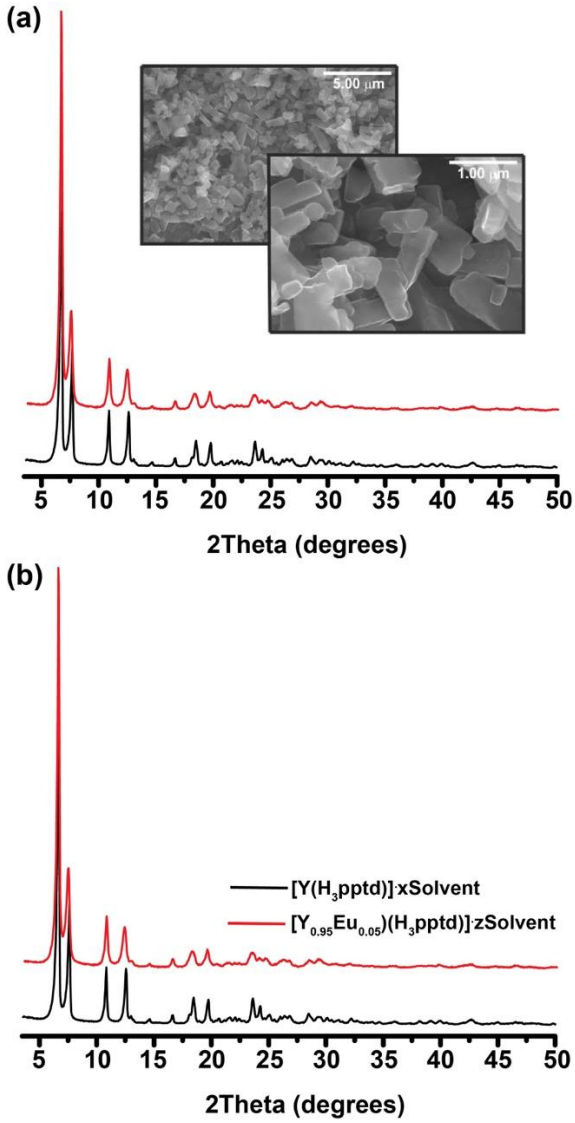

Figure 1. **(a)** Experimental (**red**) and simulated (**black**) powder X-ray diffraction patterns and SEM images of [Y(H_3pptd)]·*xSolvent* (**1**) isolated under solvothermal conditions. **(b)** Powder X-ray diffraction patterns of the isotypical [Ln(H_3pptd)]·*xSolvent* materials [where Ln^{3+} = Y^{3+} (**1**) and $(Y_{0.95}Eu_{0.05})^{3+}$ (**1_Eu**)] isolated under solvothermal conditions.

While the coordinating –PO groups are responsible for the formation of this inorganic chain, the remaining three –POH groups are directed towards the pores, forming intermolecular hydrogen bonding interactions with the crystallization solvent molecules. We emphasize that the position of these latter groups is crucial for the post-synthetic modification of this material (see the following sections for further details).

We further direct the reader to the Supporting Information which contains a whole series of structural characterization of the isotypical family of **1** (Figures S13 to S17 in the Supporting Information).

We note herein the remarkable structural robustness of the framework which, after evacuation, remains crystalline up to *ca.* 400 ºC (Figure S13 in the Supporting Information), with the synthetic approaches being amenable to the incorporation of optically-active lanthanide centres into the Y^{3+}-based network and also to an acid-base reaction as post-synthetic modification.

2.3. Post-synthetic modification: *in situ* acid-base reaction

We have post-synthetically modified **1** and **1_Eu** by replacing the protons of the free –POH moieties with extra-framework K^+ cations. The treatment with an ethanolic solution of KOH (0.05 M) led to the ion-exchanged materials $[K_3(Y)(pptd)]\cdot z$*Solvent* (**1K**) and $[K_3(Y_{0.95}Eu_{0.05})(pptd)]\cdot z$*Solvent* (**1K_Eu**) (see Experimental Section in the Supporting Information for details on the procedure and all the related structural characterization). Because in this contribution most of the studies were performed in **1_Eu** and **1K_Eu**, these materials will be discussed in more detail.

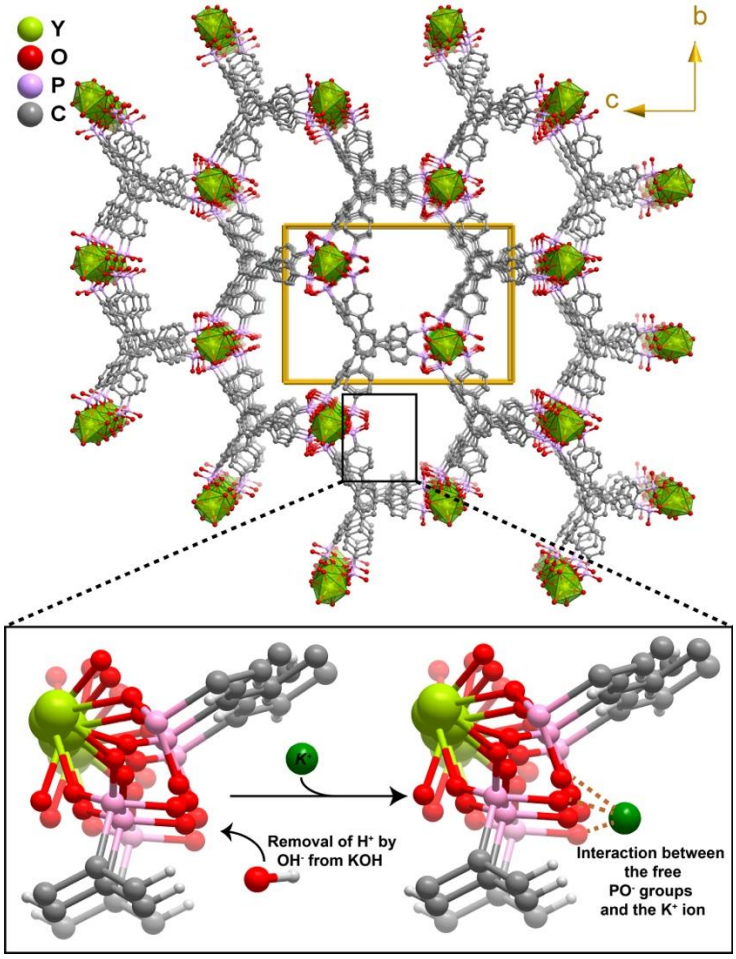

Figure 2. (*top)* Schematic representation of the crystal packing of $[Y(H_3pptd)]\cdot x$*Solvent* (**1**) viewed in perspective along the [100] direction of the unit cell. *(bottom)* Representation of the post-synthetic modification of **1** into **1K.** *Please note*: crystallization solvent molecules have been removed for clarity purposes, and the interactions between the K^+ ion and PO^- groups are solely given for illustrative purposes (local charges are not balanced).

Powder X-ray diffraction studies show that **1_Eu** and **1K_Eu** have, nevertheless, different crystalline structures, though they may be closely related to each other (Figure 3). Structural modification is assumed to be driven by distortion of the framework of **1_Eu** promoted by the inclusion of extra-framework K^+ cations. Although the crystal structure of **1K_Eu** could not be unveiled from crystallographic studies, we believe that, based on advanced characterization techniques, the most significant structural modification resides in the replacement of H^+ (belonging to the free –POH moieties) by K^+ (Figure 2, *bottom*). This fact is strongly corroborated from the FT-IR spectroscopic studies of **1_Eu** and **1K_Eu** (Figure S18 in the Supporting Information): the incorporation of K^+ leads to a clear modification of the *ca.* 1300-900 cm^{-1} spectral range, keeping the rest of the spectrum almost unchanged (despite slight shifts of some vibrational bands). The most relevant difference concerns the disappearance of the ν(P-OH) stretching vibration centred at *ca.* 923 cm^{-1} and the appearance of a sharp band, with very strong intensity, in the spectrum of **1K_Eu** at *ca.* 995 cm^{-1}, which can be attributed to the ν(P-O^-) vibrational mode.[69] Electron microscopy (SEM mapping and EDS spectrum, Figures S21 to S23 in the Supporting Information) also shows that the K^+ cations are homogeneously distributed in the structure of **1K_Eu**, with the Y^{3+} : K^+ ratio being *ca.* 1 : 2.5 (close to the expected 1 : 3), indicating that the hydrogen atoms of the –POH groups were fully replaced by K^+ cations. The information arising from the computational studies, which are discussed below, are supportive of this hypothesis.

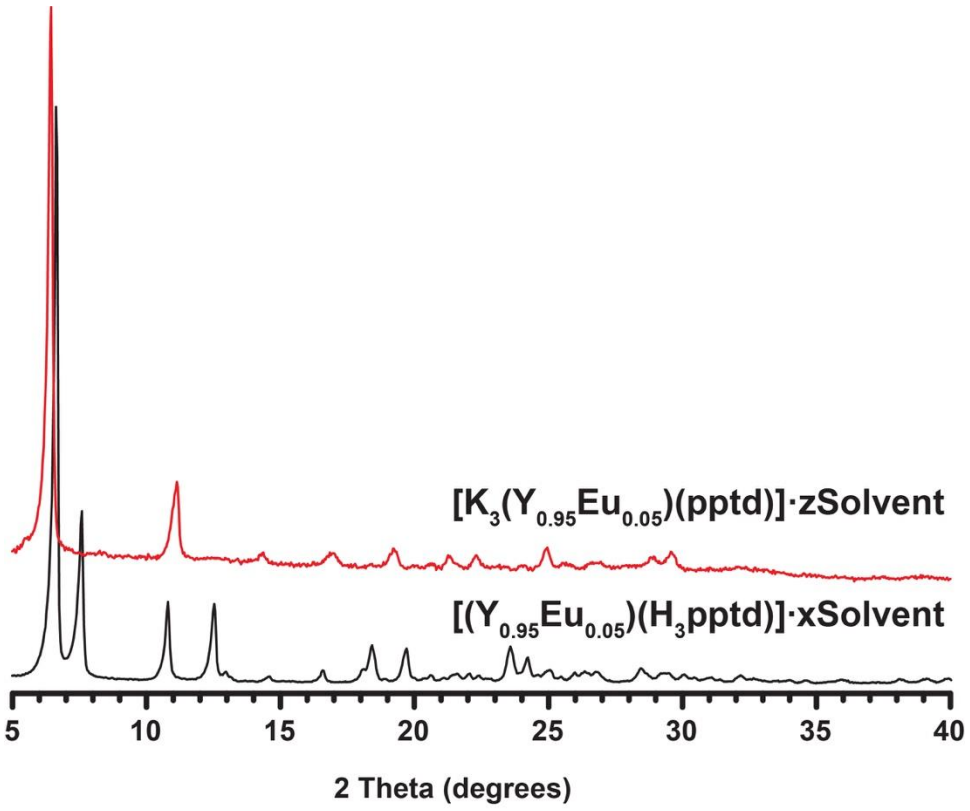

Figure 3. Powder X-ray diffraction patterns of compounds $[(Y_{0.95}Eu_{0.05})(H_3pptd)]\cdot$*xSolvent* (**1_Eu**) and $[K_3(Y_{0.95}Eu_{0.05})(pptd)]\cdot$*zSolvent* (**1K_Eu**).

The thermal behaviour of **1K_Eu** is slightly different concerning the first weight loss: it is well visible a slower kinetics for the release of the solvent molecules, probably due to a strong affinity between the extra-framework K^+ cations with, mainly, water molecules. As observed for **1_Eu**, compound **1K_Eu** remains thermally stable up to approximately 400 ºC (Figure S19 in the Supporting Information). The ^{31}P MAS spectrum of the parental ion-exchanged $[K_3Y(pptd)]\cdot z$*Solvent* (**1K**) shows three resonances centred at *ca.* 0.9, 2.5 and 3.2 ppm (Figure S20 in the Supporting Information) showing, on the one hand that the material remains crystalline (as observed from powder X-ray diffraction studies) and, on the other, that a modification in crystal symmetry must have occurred (most likely to a space group/crystal system with less symmetry elements).

3. Gas Adsorption and Separation

3.1. Static gas adsorption experiments

The accessibility of probe molecules into the porous frameworks of **1_Eu** and **1K_Eu** was evaluated from adsorption isotherms of N_2 at 77 K (Figure S24 in the Supporting Information) and CO_2 at 195, 273 and 298 K (Figure 4). **1_Eu** and **1K_Eu** materials have pores accessible to both N_2 (77 K) and CO_2 (195 K). Nevertheless, results agree with a rather slow diffusion of N_2 through the pores of those materials, more evident in the latter one which should be related to narrower pore windows. By contrast, the equilibrium of CO_2 adsorption is achieved quite rapidly, reaching an adsorption capacity of *ca.* 7.3 mmol g^{-1} and *ca.* 6.7 mmol g^{-1} at 0.3 p/p_o and 195 K, for **1_Eu** and **1K_Eu**, respectively. Noteworthy, the slope of the CO_2 adsorption isotherms in the low-pressure region for **1K_Eu** is much steeper when compared to that of **1_Eu**, with this difference becoming more visible at higher temperatures. The limited accessibility of the probe N_2 molecules to the pores of **1_Eu** and **1K_Eu** when compared to CO_2 should be associated to narrow pore windows and to the low kinetics energy of the N_2 molecules at 77 K when compared to CO_2 at 195 K. Indeed, diffusion limitations of N_2 at 77 K are not an uncommon feature, being typical of ultramicroporous materials with pore size < 0.5 nm.[70] Taking this into account, the BET surface area has been determined from the CO_2 adsorption isotherms at 195 K, accounting for 566 and 498 $m^2\ g^{-1}$ for **1_Eu** and **1K_Eu**, respectively. The adsorption capacity of CO_2 per formula unit is 4.6 and 5.0 mmol $mmol^{-1}$ for **1_Eu** and **1K_Eu**, respectively. These results clearly indicate that the incorporation of K^+ ions does not significantly reduce the inner surface of the framework, promoting instead a considerable strengthening of the interaction with CO_2. This is particularly obvious in the low pressure range at higher temperatures: CO_2 adsorption isotherms measured at 298 K (Figure 4) show that the post-synthetic modification with KOH boosts the adsorption capacity from an almost negligible 0.14 mmol g^{-1} (for **1_Eu**) to 1.9 mmol g^{-1} (for **1K_Eu**) at 0.14 bar (Figure 4). The modification of the adsorption properties upon the KOH treatment should be related to the charge polarization effect exerted by the extra framework K^+ ions. Also, the subsequently basification of the pore walls related to the deprotonation of the phosphonate residues is of great interest for post-combustion carbon capture considering the typical CO_2 partial pressure in flue gas (see below).

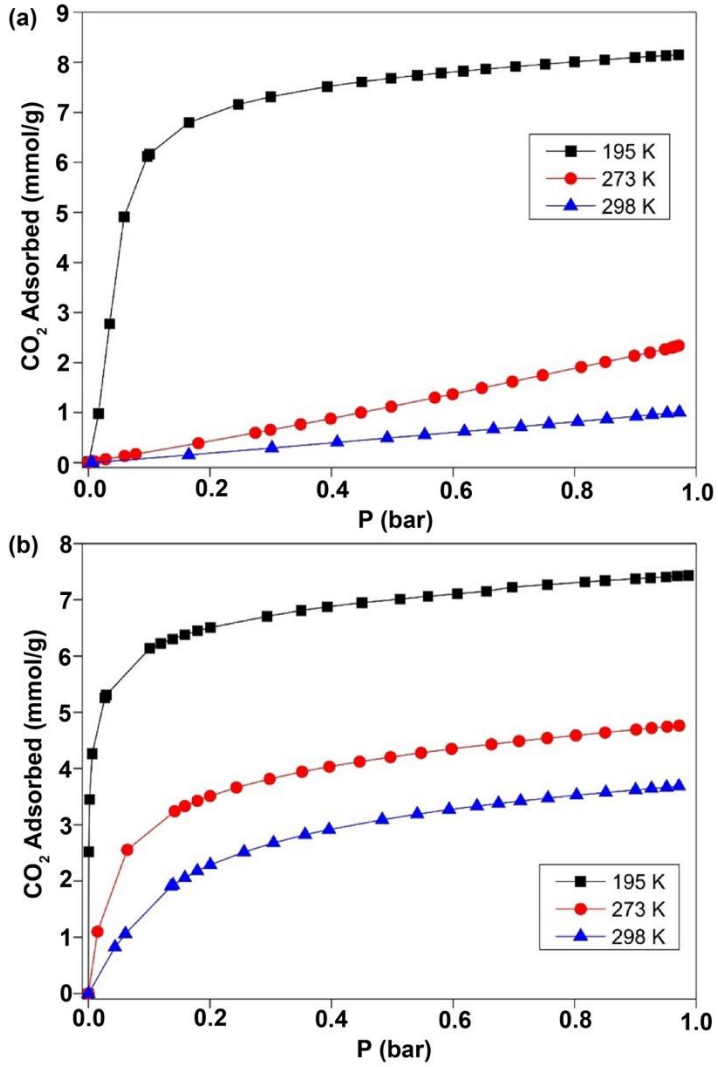

Figure 4. CO_2 adsorption isotherms measured at different temperatures for (**a**) $[(Y_{0.95}Eu_{0.05})(H_3pptd)]\cdot x\textit{Solvent}$ (**1_Eu**) and (**b**) $[K_3(Y_{0.95}Eu_{0.05})(pptd)]\cdot z\textit{Solvent}$ (**1K_Eu**).

To further investigate the effect of ion exchange on the CO_2 interaction we have calculated the isosteric heats of CO_2 adsorption for **1_Eu** and **1K_Eu**, according to the Clausius-Clapeyron equation (Eq. 1) from the adsorption isotherms measured at 273 and 298 K:

$$q_{st} = -R[\Delta(lnP)/\Delta(1/T)]_N \qquad \text{(Eq. 1)}$$

where q_{st}, R, P, T and *N* correspond to isosteric heat of adsorption, gas constant, pressure, temperature and amount of adsorbed CO_2, respectively. Results show a significant increase in the isosteric heats of adsorption of CO_2 on passing from **1_Eu** (-20.8 to -21.8 kJ mol^{-1}) to **1K_Eu** (-33.2 to -38.7 kJ mol^{-1}) which should be related to the charge polarization effects exerted by the extra framework K^+ ions and pore walls basification after hydrogen phosphonate deprotonation.[71] A related enhancement in CO_2 interaction can be found in the $[Ni_8(OH)_4(H_2O)_2(benzenebipyrazolate)_6]$ systems after treatment with KOH to yield defective

$K_x[Ni_8(OH)_6(benzenebipyrazolate)_{6-y}]$,[72] and amine functionalized MOF-74 type systems[73] showing cooperative behaviour between metal cation and basic sites interactions with CO_2 molecules.

3.2. Pulse gas chromatography experiments

In view of the significant improvement of the interaction of the CO_2 adsorbate with the porous framework after the ion exchange process, we thought that this material could shine in gas separation processes. With this aim, we have prepared chromatographic columns packed with each material and we proceed to carry out pulse gas chromatographic studies in the 273-523 K temperature range for two different gaseous ternary mixtures: $C_2H_2/CO_2/H_2$ and $C_3H_6/C_3H_8/H_2$, using a 20 mL min^{-1} flow of He as carrier gas (see Supporting Information for more experimental details).

Pulse gas chromatography studies for an equimolar mixture of $C_2H_2/CO_2/H_2$, performed at different temperatures using **1_Eu**, showed that both C_2H_2 and CO_2 (quadrupolar gas molecules) interact with its porous framework (Figure S25 in the Supporting Information). Chromatograms showed that CO_2 eluted before C_2H_2 indicating that the latter molecule interacts more strongly than the former one with **1_Eu**. For $C_3H_6/C_3H_8/H_2$ gas mixtures, propylene has a higher affinity to **1_Eu** than propane (Figure S28 in the Supporting Information). Remarkably, an opposite gas selectivity behaviour was observed for **1K_Eu**. Indeed, the injection of an equimolar mixture of C_2H_2/CO_2 shows that C_2H_2 elutes before CO_2 (Figures S26 and S27 in the Supporting Information) which agrees with CO_2 having a significant higher affinity to **1K_Eu** material than C_2H_2. It should be highlighted, however, that the heat of adsorption values disagree with that obtained from single component adsorption isotherms (see above), which might be attributed to the differences in the nature of the experiment, namely the low pressure region for the pulse gas studies with the CO_2 molecules interacting with the most active basic sites of the surface, due to the formation of carbonates (see Figure S30 in the Supporting Information for further details).[72] We note that these results are well compatible with breakthrough curve measurements and density functional theory (DFT) calculations that reveal very similar adsorption energies for CO_2 and C_2H_2 (see below).

The inclusion of K^+ and the concomitant creation of PO_3^{2-} basic sites justifies the significant improvement in the selective adsorption of acidic CO_2. Additionally, the interaction between C_2H_2 and **1K_Eu** also increases, but this improvement is not as significant. This result might relate to the fact that the basicity of phosphonate residues ($pKa_2 \sim 6.9$)[74] is not enough to give rise to a significant acid-base interaction with C_2H_2 ($pKa = 25$).

3.3. Gas separation breakthrough studies

Breakthrough curves were measured to evaluate the performance of **1_Eu** and **1K_Eu** in the separation of bulk gas mixtures. Results confirm that **1K_Eu** exhibits higher interaction for CO_2 and C_2H_2 than **1_Eu** giving rise to increasing adsorption capacities on passing from **1_Eu** to **1K_Eu**, being the former gas more retained when the complex ternary mixture $CO_2/C_2H_2/CH_4$ was flowed through the column (Figure S34 in the Supporting Information). On the other hand, C_3H_6 and C_3H_8 are efficiently more

adsorbed into the framework of **1_Eu** than **1K_Eu** with C_3H_6 exhibiting a stronger interaction with **1_Eu** (Figure S40 in the Supporting Information). For more details regarding these preliminary studies we direct the reader to the dedicated Section in the Supporting Information.

Because **1K_Eu** efficiently and selectively retains CO_2, breakthrough experiments were scaled up in order to improve and study this feature. For that, a homemade stainless-steel column (Figure S31 - *right* in the Supporting Information) was packed with 2.31 g of **1K_Eu** (*ca.* 4.8 times more than the amount, *i.e.* 0.48 g, used in the preliminary studies; see Supporting Information for further details). CO_2/N_2 (3 mL min^{-1} : 17 mL min^{-1}) breakthrough curves show that, as in the preliminary studies, N_2 is not retained into the framework of **1K_Eu**, while CO_2 is effectively adsorbed with amounts of 2.60, 1.62, 1.23 and 1.03 mmol g^{-1} at 273, 298, 303 and 323 K, respectively (Figure S45 in the Supporting Information). **1K_Eu** is remarkably capable to retain CO_2 even at higher temperatures, namely 323 K, which is the typical working condition of a flue gas emission from a fossil fuel power plant. In order to show the suitability of this material for practical applications, we have investigated the reversibility of the CO_2 capture by **1K_Eu** in ten consecutive breakthrough cycles flowing the binary gas mixture CO_2/N_2 (3 mL min^{-1} : 17 mL min^{-1}), i.e. through the column packed with 2.31 g of **1K_Eu** (Figure S31 - right in the Supporting Information), at 323 K. Despite the slight decrease in the adsorption capacity of **1K_Eu** from the first to the second breakthrough cycle, probably due to a partial chemisorption of CO_2 in the most active adsorptive sites (see above), the process is highly reproducible in the subsequent cycles with the reactivation of the material being easily carried out at 353 K (Figure 5). In this regard, the energy penalty of the present CO_2 capture process is considerably lower than the traditional use of amine solutions.[75] In order to further show the suitability of this material for this separation process, similar measurements were carried out under humid conditions, in order to reproduce the conditions of a flue gas emission from a power plant.[76] Noteworthy, **1K_Eu** is able to retain CO_2 under humid conditions (0.86 CO_2 mmol g^{-1}); however, the adsorption capacity slightly decreases over the following cycles down to 0.56 CO_2 mmol g^{-1} in the 5^{th} cycle (Figure S46 in the Supporting Information). This result might be attributed to the highly hydrophilic nature of the pores as illustrated from water adsorption isotherms (Figure S56 in the Supporting Information).

To further prove the gas adsorption selectivity of **1K_Eu**, the gas separation performance was evaluated towards the separation of complex ternary gas mixture composed of CH_4 (14 mL min^{-1}), CO_2 (3 mL min^{-1}) and C_2H_2 (3 mL min^{-1}) in the temperature range 273-323 K. While CH_4 is not retained in the column, C_2H_2 and CO_2 exhibit strong interactions with **1K_Eu**, being CO_2 the most strongly retained gas molecule (Figures 6 and S47 in the Supporting Information). The separation of C_2H_2 from CO_2 is more efficient when a larger amount of **1K_Eu** is used (Figures S38 and S47 in the Supporting Information). The scale-up of **1K_Eu** allows an efficient separation of C_2H_2 from CO_2 even at higher temperatures (Figure 6). In short, the ability of **1K_Eu** to separate C_2H_2 from CO_2 is truly remarkable: we note that this separation is extremely difficult as a consequence of the similarity in size, shape and physical properties of both gases.[71,77] Moreover, the observed stronger interaction of CO_2 over C_2H_2 with the **1K_Eu** host framework

is rather unusual. In this regard, most of the reported examples exhibit the reverse selectivity with stronger interactions of C_2H_2 over CO_2 as a consequence of cooperative supramolecular interactions with the host framework[77] and/or bonding to coordinatively unsaturated metal centers.[78] We have previously observed a slightly higher interaction of CO_2 over C_2H_2 at high temperature (323 K) with the $NH_4[Cu_3(\mu_3\text{-OH})(\mu_3\text{-4-carboxypyrazolato})_3]$ framework, which was attributed to charge gradient interactions.[71] Noteworthy, the much higher selectivity of CO_2 over C_2H_2 for **1K_Eu** in the whole studied temperature range might be attributed to a cooperative effect of basicity increase of deprotonated phosphonate groups and charge gradients upon K^+ incorporation into the framework.

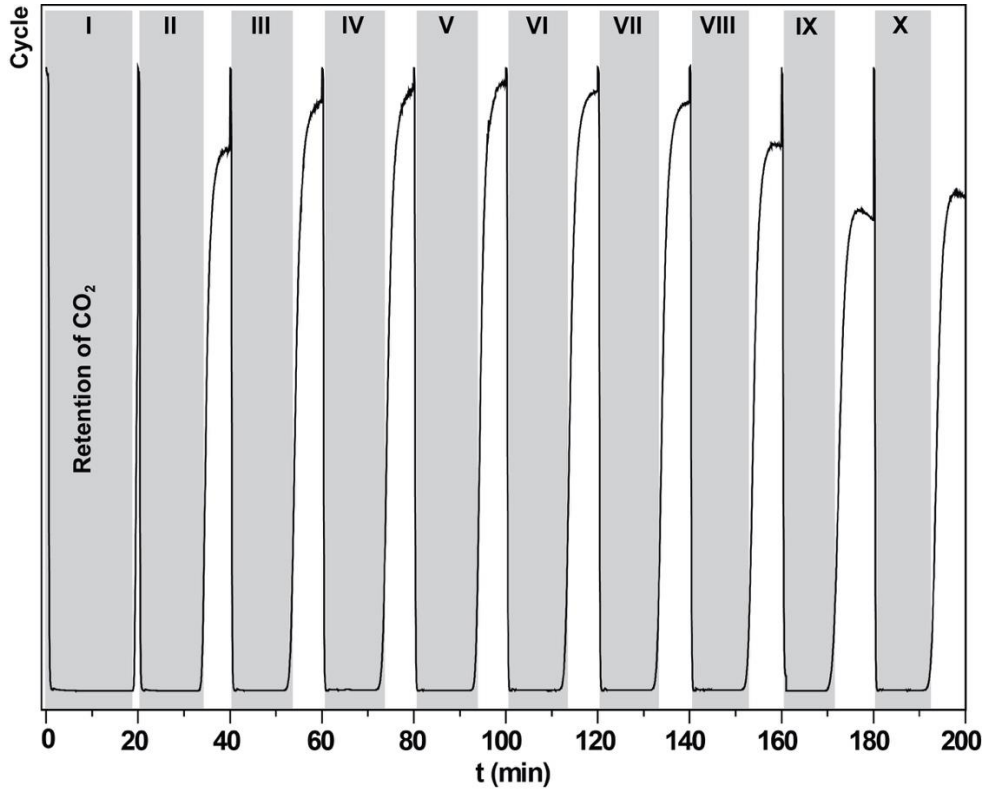

Figure 5. Ten successive CO_2/N_2 breakthrough cycles of $[K_3(Y_{0.95}Eu_{0.05})(pptd)]\cdot z$*Solvent* (**1K_Eu**) measured at 323 K followed by reactivation at 353 K. Grey regions represent the periods of time in which CO_2 is retained. Experiments were performed by flowing the binary gas mixture CO_2/N_2 (3 mL min^{-1} : 17 mL min^{-1}), through the column packed with 2.31 g of **1K_Eu**.

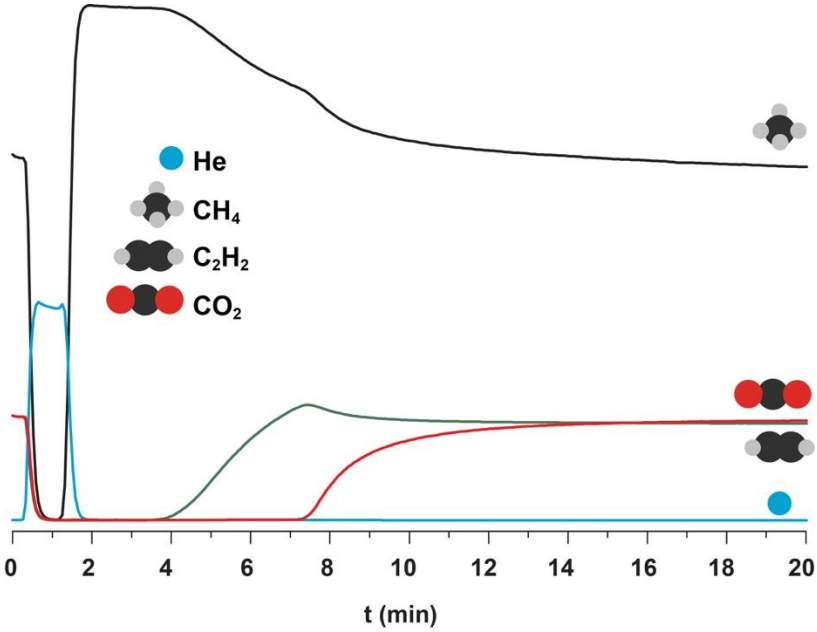

Figure 6. $CO_2/C_2H_2/CH_4$ breakthrough curves measured at 323 K for $[K_3(Y_{0.95}Eu_{0.05})(pptd)]\cdot z$*Solvent* (**1K_Eu**). Experiments were performed by flowing a ternary gas mixture $CO_2/C_2H_2/N_2$ (3 mL min^{-1}: 3 mL min^{-1}:14 mL min^{-1}), through the column packed with 0.48 g of **1K_Eu**. Color code: He (cyan), CH_4 (black), CO_2 (red), C_2H_2 (green).

4. Computational Studies

Computer simulations were also performed to obtain further structural information about the **1_Eu** and **1K_Eu** materials. The experimental crystallographic cell for **1_Eu**, with hydrogen positions refined by density functional theory (DFT) was used in grand canonical Monte Carlo (GCMC) simulations for calculating the adsorption isotherm of CO_2 at T = 298.15 K (please refer to the Supporting Information for details). As depicted in Figure 7, there is a slight but systematic overestimation in the entire pressure range of the simulated adsorbed amount (red line with full symbols) of CO_2 in **1_Eu** relative to the experimental one (black line with full symbols). This may be due to impurities, defects, or residual solvent in the experimental sample, which cause a reduction in the available pore volume. In fact, simulations are based on a perfect crystalline framework, where these problems are absent. We have used the Poreblazer code[79] to calculate the surface area of the perfect crystallographic cell and the value obtained, 836 m^2/g, also overestimates the experimental one, 566 m^2/g. The latter value is ~0.68 times the former one. Therefore, we have used this information to scale the computed adsorbed amounts of CO_2 in **1_Eu** and the resulting isotherm (green line with full symbols in Figure 7) compares quite satisfactorily with the experimental data.

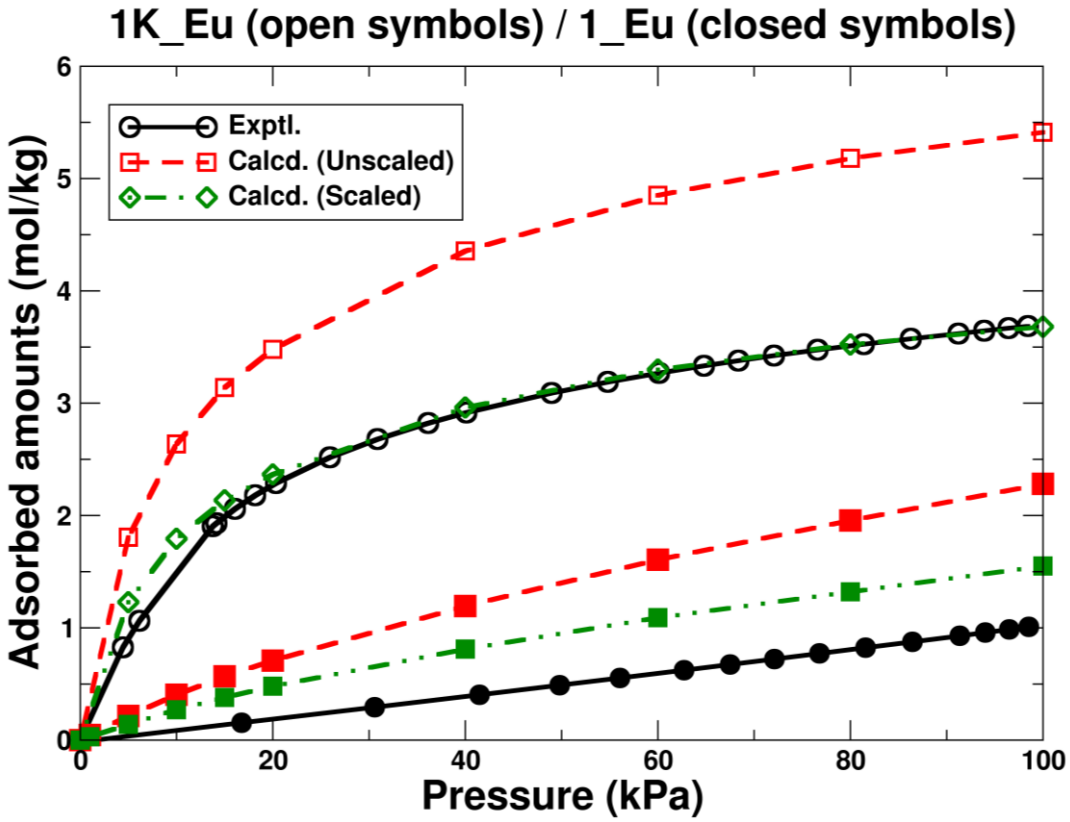

Figure 7. Experimental (full) and calculated (dashed) CO_2 adsorption isotherms for **1_Eu** (closed symbols) and **1K_Eu** (open symbols) at T = 298.15 K. Scaled curves (dot-dashed lines) were obtained from the unscaled (dashed lines) ones upon multiplication by 0.68 (see text for details).

The experimental cell for **1_Eu** but with protons exchanged by potassium cations was used to calculate the adsorption isotherm for CO_2 in **1K_Eu**. Atomic positions were optimized by DFT (details in the Supporting Information). As presented in Figure 7, the calculated adsorption isotherm (red line with open symbols) also overestimates the experimental one (black line with open symbols) but a very encouraging agreement is found after scaling the adsorbed amounts by 0.68 (green curve with open symbols). This result suggests that the crystallographic structure for the **1K_Eu** shares strong similarities with that of **1_Eu**, though it could never be determined exactly during our experimental studies. Views of these two structures are provided in Figure S48 where it is possible to see that the K^+ cations in **1K_Eu** stay close to the positions occupied by the protons in **1_Eu**, but with distances to the oxygen atoms increasing from ~1.0 Å in **1_Eu** to 2.6-2.8 Å in **1K_Eu**. In addition, we provide as Supporting Information two movies and several snapshots depicted in Figures S53 and S54: for a pressure of 10 kPa, the increased CO_2 adsorption capacity displayed by **1K_Eu** is dictated by the presence of K^+ as most adsorbate molecules are found in their vicinity.

Table 1. Calculated adsorption energies (kJ/mol) for CO_2 adsorption in **1_Eu** and **1K_Eu**. Values outside (inside) parenthesis were computed with the PBE-D3BJ (vdW-DF2) approach.

Gas	**1_Eu**	**1K_Eu**
CO_2	-37.0 (-41.6)	-41.2 (-48.5)
C_2H_2	-37.8 (-35.6)	-50.6 (-51.6)
C_3H_6	-44.7 (-48.8)	-66.4 (-68.0)
C_3H_8	-48.6 (-59.2)	-52.3 (-54.5)

DFT calculations were performed for computing the energies of adsorption of CO_2 in the two materials which are compiled in Table 1. The calculated values for **1K_Eu** are 4.2 kJ/mol (PBE-D3BJ) or 6.9 kJ/mol (vdW-DF2), more negative (*i.e.*, more favorable, equation S1) than in **1_Eu**. The more favorable adsorption in **1K_Eu** can be associated to, on the one hand, the existence of close contacts between the carbon atom of CO_2 and the neighboring negatively charged framework oxygen atoms and, on the other hand, between the oxygen atoms of CO_2 and neighboring positively charged framework potassium species (Figures 8 and S49 in the Supporting Information); the shorter interactions in **1_Eu** involve polarized oxygen and hydrogen atoms. The calculations were further extended to C_2H_2, C_3H_6 and C_3H_8 gases, with the energies being compiled in Table 1, and schematic representations of the optimized geometries provided in Figures S50-S52 (in the Supporting Information), respectively. We note that, for both **1_Eu** and **1K_Eu**, the DFT calculations predict that C_2H_2 has adsorption energies similar to those calculated for CO_2. Interestingly, in general, the energies for C_2H_2 are slightly more negative than those calculated for CO_2. Consequently, although the general trend of increasing interactions of guest molecules with the host framework on passing from **1_Eu** to **1K_Eu** can be clearly modelled, the subtle changes in the interaction of CO_2 *vs* C_2H_2 explaining the adsorption selectivity may be attributed to the different adsorption arrangements found for these two molecules. In fact, contrarily to what happens with CO_2 that adsorbs nearby the walls of the **1K_Eu** adsorbent, acetylene adsorbs in the middle of the channel (Figure S50 in the Supporting Information). The stabilization of the latter molecule is promoted by the contacts between its hydrogen atoms and the oxygen atoms belonging to the MOF framework. Therefore, from the different adsorption arrangements it seems that more CO_2 molecules can interact more favorably with the adsorbent walls when compared to C_2H_2. Additionally, as can be concluded from the very large (under humid conditions) experimental adsorption energies for CO_2 in **1K_Eu** when compared with all the other adsorbates studied (Table S2), some CO_2 molecules seem to form other carbonaceous species inside the pores of **1K_Eu**. Such species are very stable, and no desorption was found under the conditions used in the adsorption experiments. An in-depth clarification of this hypothesis requires substantial work, *e.g.*, the combination of computer simulations and sophisticated experimental solid-state NMR as in previous studies devoted to the understanding of CO_2 adsorption by aminated silicas.[80-81]

In the case of propane and propylene, the observed trend of increasing adsorption interactions on passing from **1_Eu** to **1K_Eu** is maintained but dependent on the DFT exchange-correlation functional considered. Moreover, the calculated adsorption energies are more negative than in the cases of CO_2 and C_2H_2, mainly because of favorable van der Waals contacts with the organic moieties of **1_Eu** and **1K_Eu**, as illustrated in Figures S51 and S52, (in the Supporting Information), respectively. The double bond of propylene interacts with a K^+ ion when adsorbing in **1K_Eu**, with a concomitant stabilization on going from **1_Eu** to **1K_Eu** (Figures S51).

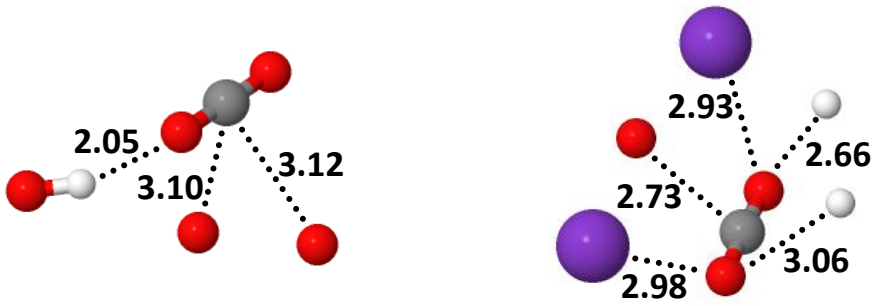

Figure 8. Schematic representation of the close contacts (dotted lines) between CO_2 and the frameworks of (*left*) **1_Eu** and (*right*) **1K_Eu**. Values correspond to distances in Å. Color code for spheres: H, white; C, grey; O, red; and K, purple.

5. Ionic Conduction Studies

The presence of phosphonate-containing organic moieties as proton carriers and hydrogen bonded chains embodies the $[(Y_{0.95}Eu_{0.05})(H_3pptd)]\cdot x$*Solvent* (**1_Eu**) and $[K_3(Y_{0.95}Eu_{0.05})(pptd)]\cdot z$*Solvent* (**1K_Eu**) solids with potentially high proton conductivity. The mechanism of ion conduction is mainly influenced by the structure of the materials, temperature, concentration, and mobility of the charge carriers.

The pellets employed for the electrical measurements could be easily pressed free from major defects while preserving the crystallinity of the materials. The Nyquist plots for **1_Eu** and **1K_Eu** at 40% and 98% RHs show that the bulk resistance of both materials decreases while increasing the RH (Figure S55 in the Supporting Information). Considering that the structure of **1K_Eu** must share many similarities with that of **1_Eu**, and that both materials have not so different surface area, one can infer that the higher conductivity of **1K_Eu** arises from the presence of K^+ cations. Arrhenius plots of the electrical conductivity of **1_Eu** and **1K_Eu** collected under variable RH are depicted in Figure 9. The conductivity for both materials is clearly humidity dependent, similar to that reported for water-mediated ionic conductors.[50] This suggests that both materials are able to absorb molecular water to favor the proton transportation. **1K_Eu** exhibits a proton conductivity value of 1.89×10^{-1} S cm^{-1} at 94 ºC and 98% RH, which is more than 4 orders of magnitude higher than that of **1_Eu** (1.24×10^{-5} S cm^{-1}) under the same conditions. This is, in itself, an outstanding value in respect to other proton-conducting materials that also present bulk conductivities over

than 10^{-1} S cm^{-1} under similar conditions.[50-54] The range of activation energies (*E*a) obtained from the Arrhenius plots for both materials is in line with those reported for other MOFs.[51] The *E*a in **1_Eu** are in the range of 42-56 kJ mol^{-1} for 20-98% RH and in the case of **1K_Eu** the *E*a are lower than for **1_Eu** at RH ≤ 80% (23-27 kJ mol^{-1}) and increase for RH near saturation (*E*a of 62 kJ mol^{-1}). These results suggest that charge transport mainly occurs through structural diffusion, and for saturated conditions the increase in energy associated to the conductivity in **1K_Eu** may be explained by the exchange of K^+ cations into the conduction medium. On the other hand, the conductivity in **1_Eu** is likely to result solely from proton transport, given the acidic nature of the phosphonate groups. The water vapor isotherms for both materials (Figure S56 in the Supporting Information) are in agreement with the conductivity results, if one considers that **1K_Eu** adsorbs more water, conferring it increased conductivity. However, the water excess adsorbed by **1K_Eu** in comparison to **1_Eu** (about the double) cannot explain the three to four orders of magnitude conductivity enhancement. These results further suggest that the high ionic conductivity of **1K_Eu** is the result of the contribution of other ionic species than protons in hydronium ions, which most likely are K^+. Besides the effect of the enhanced charge carrier concentration, the presence of water in **1K_Eu** can strongly enhance the mobility of these cations in the pores.

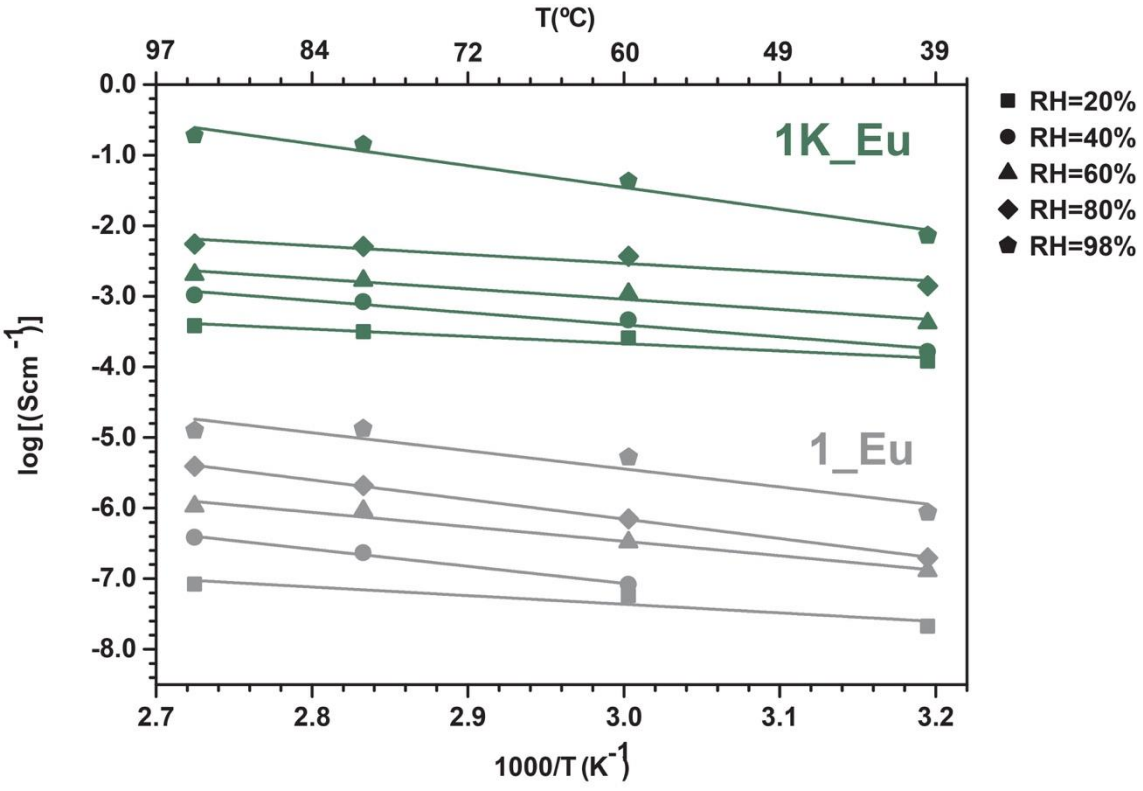

Figure 9. Arrhenius plots of the conductivity for $[(Y_{0.95}Eu_{0.05})(H_3pptd)]\cdot x$*Solvent* (**1_Eu**) and $[K_3(Y_{0.95}Eu_{0.05})(pptd)]\cdot z$*Solvent* (**1K_Eu**) under variable relative humidity conditions (RH).

6. General Considerations and Conclusions

We have successfully shown the remarkable effect that the acid-base post-synthetic modification of a robust porous phosphonate-based network has in the overall properties of the material. [Ln(H_3pptd)]·*x*Solvent [where Ln^{3+} = Y^{3+} (**1**) and $(Y_{0.95}Eu_{0.05})^{3+}$ (**1_Eu**)], prepared using various synthetic methods (some capable of a scale-up at moderate conditions) from the highly rigid (5'-(4-phenylphosphonic acid)-[1,1':3',1''-terphenyl]-4,4''-diyl)diphosphonic acid (**H_6pptd**), was transformed into [K_3Ln(pptd)]·z*Solvent* [where Ln^{3+} = Y^{3+} (**1K**) and $(Y_{0.95}Eu_{0.05})^{3+}$ (**1K_Eu**)] by immersing the powder of **1** into an ethanolic solution of KOH for 48h. Notably, the incorporation of K^+ cations into the framework of **1** proved to be a crucial step for the significant improvement of the various properties studied. While this improvement is more evident in the proton conduction studies, it is notably present as well in both the CO_2 adsorption and gas separation. **1K_Eu** shows a CO_2 adsorption of 17.3 wt% (4.76 mmol g^{-1}) and 13.9 wt% (3.68 mmol g^{-1}) at 273 and 298K, respectively. While these values are above average when compared to other reported materials, we stress above all the considerable increase after the post-synthetic incorporation of K^+ cations. At ambient temperature, the adsorption of CO_2 increased by 3-fold (from 4.24 to 13.9 wt%), with adsorption values rivalling with many reported MOF materials improved by incorporation with amine groups. Another important feature of this modification refers to the separation process of different gases in the presence of N_2 (see Table S3 in the Supporting Information for further details). Both materials show separation capabilities of CO_2, C_2H_2, C_3H_6 and C_3H_8 from N_2. **1Eu** displays an increase separation of C_3H_6 when compared to the other gases (CO_2 has a negligible adsorption of 0.18 mmol g^{-1}), while **1K_Eu** performs better in retaining CO_2 than **1Eu**, even separating these two gases at higher temperatures (303 and 323 K).

This improvement was more relevant in the proton conduction studies. While **1_Eu** shows typical conductivity values for phosphonate-based MOFs, reaching 1.24×10^{-5} S cm^{-1} at 94 ºC and 98% RH, the inclusion of K^+ cations increased the conductivity by four orders of magnitude, with final values at 94 ºC and 98 % RH reaching 1.89×10^{-1} S cm^{-1}. We stress that this increase makes this new material to reach current top 5 most conducting MOFs,[82-83] with conductivities higher than Nafion (or even MOFs-impregnated Nafion membranes),[84] and of the best phosphonate-based MOF by orders of magnitude in the 1000-10000 range.[85] In fact, looking at the Arrhenius plots in Figure 8 one can see that **1K_Eu** has higher conductivities at low humidity and temperature (1.23×10^{-4} S cm^{-1} at 40 ºC and 20% RH) than **1_Eu** at saturated conditions. This is unequivocal evidence that the post-synthetic incorporation can be employed as a useful tool to improve the properties of MOFs so they can be used in fuel cells under relatively mild conditions.

In short, we have unequivocally demonstrated that robust porous LnOFs based on phosphonate-based ligands can be prepared using several techniques (some at the gram scale) and that truly

multifunctional materials can be designed by simple post-synthetic modification based on the acidity of the inner walls of the porous MOF.

7. Acknowledgments

This work was developed within the scope of the project CICECO - Aveiro Institute of Materials (UIDB/50011/2020 & UIDP/50011/2020), LAQV-REQUIMTE (UIDB/50006/2020) and CQE (UIDB/00100/2020) research units, financed by national funds through the FCT/MEC and when appropriate co-financed by FEDER under the PT2020 Partnership Agreement. FCT is also gratefully acknowledged for the post-doctoral grants SFRH/BPD/94381/2013 (to S.M.F.V.) and for the Junior Research Position CEECIND/00553/2017 (to RFM). JARN thanks Spanish MINECO (CTQ2017-84692-R), Junta de Andalucia (P18-RT-612) and EU FEDER Funding. The research contract of P.B. is funded by National Funds (OE), through FCT – Fundação para a Ciência e a Tecnologia, I.P., in the scope of the framework contract foreseen in the numbers 4, 5 and 6 of article 23, of the Decree-Law 57/2016, of August 29, changed by Law 57/2017, of July 19. We would like to thank Dr Pedro Carvalho and Dr Liliana Silva (CICECO) for helping in our CO_2 adsorption experiments for the collection of FTIR-ATR data. We also wish to acknowledge the terrific help of all reviewers of the present manuscript whose comments helped to improve the quality of the work.

8. Additional information

For further details on synthetic procedures for all materials and organic linker, additional characterization of prepared and post-modified materials, additional gas sorption, computational and conductivity studies we direct the reader for the supplementary information file available in the online version of the paper. The Supporting Information is available free of charge on the ACS Publications.

References

(1) Mendes, R. F.; Figueira, F.; Leite, J. P.; Gales, L.; Almeida Paz, F. A. Metal-organic frameworks: a future toolbox for biomedicine? *Chem. Soc. Rev.* **2020**, DOI: 10.1039/D1030CS00883D.

(2) Rowsell, J. L. C.; Yaghi, O. M. Effects of functionalization, catenation, and variation of the metal oxide and organic linking units on the low-pressure hydrogen adsorption properties of metal-organic frameworks. *J. Am. Chem. Soc.* **2006**, *128*, 1304-1315.

(3) Gandara, F.; Furukawa, H.; Lee, S.; Yaghi, O. M. High Methane Storage Capacity in Aluminum Metal-Organic Frameworks. *J. Am. Chem. Soc.* **2014**, *136*, 5271-5274.

(4) Yuan, D. Q.; Lu, W. G.; Zhao, D.; Zhou, H. C. Highly Stable Porous Polymer Networks with Exceptionally High Gas-Uptake Capacities. *Adv. Mater.* **2011**, *23*, 3723-3725.

(5) Lim, D. W.; Chyun, S. A.; Suh, M. P. Hydrogen Storage in a Potassium-Ion-Bound Metal-Organic Framework Incorporating Crown Ether Struts as Specific Cation Binding Sites. *Angew. Chem.-Int. Edit.* **2014**, *53*, 7819-7822.

(6) Tranchemontagne, D. J.; Park, K. S.; Furukawa, H.; Eckert, J.; Knobler, C. B.; Yaghi, O. M. Hydrogen Storage in New Metal-Organic Frameworks. *J. Phys. Chem. C* **2012**, *116*, 13143-13151.

(7) Peng, Y.; Krungleviciute, V.; Eryazici, I.; Hupp, J. T.; Farha, O. K.; Yildirim, T. Methane Storage in Metal-Organic Frameworks: Current Records, Surprise Findings, and Challenges. *J. Am. Chem. Soc.* **2013**, *135*, 11887-11894.

(8) DeSantis, D.; Mason, J. A.; James, B. D.; Houchins, C.; Long, J. R.; Veenstra, M. Techno-economic Analysis of Metal-Organic Frameworks for Hydrogen and Natural Gas Storage. *Energy Fuels* **2017**, *31*, 2024-2032.

(9) Luo, F.; Yan, C. S.; Dang, L. L.; Krishna, R.; Zhou, W.; Wu, H.; Dong, X. L.; Han, Y.; Hu, T. L.; O'Keeffe, M.; Wang, L. L.; Luo, M. B.; Lin, R. B.; Chen, B. L. UTSA-74: A MOF-74 Isomer with Two Accessible Binding Sites per Metal Center for Highly Selective Gas Separation. *J. Am. Chem. Soc.* **2016**, *138*, 5678-5684.

(10) Pires, J.; Fernandes, J.; Dedecker, K.; Gomes, J. R. B.; Perez-Sanchez, G.; Nouar, F.; Serre, C.; Pinto, M. L. Enhancement of Ethane Selectivity in Ethane-Ethylene Mixtures by Perfluoro Groups in Zr-Based Metal-Organic Frameworks. *ACS Appl. Mater. Interfaces* **2019**, *11*, 27410-27421.

(11) Pillai, R. S.; Pinto, M. L.; Pires, J.; Jorge, M.; Gomes, J. R. B. Understanding Gas Adsorption Selectivity in IRMOF-8 Using Molecular Simulation. *ACS Appl. Mater. Interfaces* **2015**, *7*, 624-637.

(12) Padial, N. M.; Procopio, E. Q.; Montoro, C.; Lopez, E.; Oltra, J. E.; Colombo, V.; Maspero, A.; Masciocchi, N.; Galli, S.; Senkovska, I.; Kaskel, S.; Barea, E.; Navarro, J. A. R. Highly Hydrophobic Isoreticular Porous Metal-Organic Frameworks for the Capture of Harmful Volatile Organic Compounds. *Angew. Chem.-Int. Edit.* **2013**, *52*, 8290-8294.

(13) Britt, D.; Tranchemontagne, D.; Yaghi, O. M. Metal-organic frameworks with high capacity and selectivity for harmful gases. *Proc. Natl. Acad. Sci. U. S. A.* **2008**, *105*, 11623-11627.

(14) Hasan, Z.; Jhung, S. H. Removal of hazardous organics from water using metal-organic frameworks (MOFs): Plausible mechanisms for selective adsorptions. *J. Hazard. Mater.* **2015**, *283*, 329-339.

(15) Li, Y.; Wang, L. J.; Fan, H. L.; Shangguan, J.; Wang, H.; Mi, J. Removal of Sulfur Compounds by a Copper-Based Metal Organic Framework under Ambient Conditions. *Energy Fuels* **2015**, *29*, 298-304.

(16) Peng, Y. G.; Huang, H. L.; Zhang, Y. X.; Kang, C. F.; Chen, S. M.; Song, L.; Liu, D. H.; Zhong, C. L. A versatile MOF-based trap for heavy metal ion capture and dispersion. *Nat. Commun.* **2018**, *9*, Article number: 187.

(17) Tanabe, K. K.; Cohen, S. M. Engineering a Metal-Organic Framework Catalyst by Using Postsynthetic Modification. *Angew. Chem.-Int. Edit.* **2009**, *48*, 7424-7427.

(18) Gedrich, K.; Heitbaum, M.; Notzon, A.; Senkovska, I.; Frohlich, R.; Getzschmann, J.; Mueller, U.; Glorius, F.; Kaskel, S. A Family of Chiral Metal-Organic Frameworks. *Chem.-Eur. J.* **2011**, *17*, 2099-2106.

(19) Zhu, L.; Liu, X. Q.; Jiang, H. L.; Sun, L. B. Metal-Organic Frameworks for Heterogeneous Basic Catalysis. *Chem. Rev.* **2017**, *117*, 8129-8176.

(20) Fei, H. H.; Shin, J. W.; Meng, Y. S.; Adelhardt, M.; Sutter, J.; Meyer, K.; Cohen, S. M. Reusable Oxidation Catalysis Using Metal-Monocatecholato Species in a Robust Metal-Organic Framework. *J. Am. Chem. Soc.* **2014**, *136*, 4965-4973.

(21) Liu, X. G.; Wang, H.; Chen, B.; Zou, Y.; Gu, Z. G.; Zhao, Z. J.; Shen, L. A luminescent metal-organic framework constructed using a tetraphenylethene-based ligand for sensing volatile organic compounds. *Chem. Commun.* **2015**, *51*, 1677-1680.

(22) Chen, B. L.; Wang, L. B.; Zapata, F.; Qian, G. D.; Lobkovsky, E. B. A luminescent microporous metal-organic framework for the recognition and sensing of anions. *J. Am. Chem. Soc.* **2008**, *130*, 6718-+.

(23) Lustig, W. P.; Mukherjee, S.; Rudd, N. D.; Desai, A. V.; Li, J.; Ghosh, S. K. Metal-organic frameworks: functional luminescent and photonic materials for sensing applications. *Chem. Soc. Rev.* **2017**, *46*, 3242-3285.

(24) Harbuzaru, B. V.; Corma, A.; Rey, F.; Jorda, J. L.; Ananias, D.; Carlos, L. D.; Rocha, J. A Miniaturized Linear pH Sensor Based on a Highly Photoluminescent Self-Assembled Europium(III) Metal-Organic Framework. *Angew. Chem.-Int. Edit.* **2009**, *48*, 6476-6479.

(25) Zhang, M.; Feng, G. X.; Song, Z. G.; Zhou, Y. P.; Chao, H. Y.; Yuan, D. Q.; Tan, T. T. Y.; Guo, Z. G.; Hu, Z. G.; Tang, B. Z.; Liu, B.; Zhao, D. Two-Dimensional Metal-Organic Framework with Wide Channels and Responsive Turn-On Fluorescence for the Chemical Sensing of Volatile Organic Compounds. *J. Am. Chem. Soc.* **2014**, *136*, 7241-7244.

(26) Carrasco, S. Metal-Organic Frameworks for the Development of Biosensors: A Current Overview. *Biosensors-Basel* **2018**, *8*, 30.

(27) Imaz, I.; Rubio-Martinez, M.; Garcia-Fernandez, L.; Garcia, F.; Ruiz-Molina, D.; Hernando, J.; Puntes, V.; Maspoch, D. Coordination polymer particles as potential drug delivery systems. *Chem. Commun.* **2010**, *46*, 4737-4739.

(28) McKinlay, A. C.; Allan, P. K.; Renouf, C. L.; Duncan, M. J.; Wheatley, P. S.; Warrender, S. J.; Dawson, D.; Ashbrook, S. E.; Gil, B.; Marszalek, B.; Duren, T.; Williams, J. J.; Charrier, C.; Mercer, D. K.; Teat, S. J.; Morris, R. E. Multirate delivery of multiple therapeutic agents from metal-organic frameworks. *APL Mater.* **2014**, *2*, Article Number: 124108.

(29) Della Rocca, J.; Liu, D. M.; Lin, W. B. Nanoscale Metal-Organic Frameworks for Biomedical Imaging and Drug Delivery. *Accounts Chem. Res.* **2011**, *44*, 957-968.

(30) Zheng, H. Q.; Zhang, Y. N.; Liu, L. F.; Wan, W.; Guo, P.; Nystrom, A. M.; Zou, X. D. One-pot Synthesis of Metal Organic Frameworks with Encapsulated Target Molecules and Their Applications for Controlled Drug Delivery. *J. Am. Chem. Soc.* **2016**, *138*, 962-968.

(31) Shalini, S.; Dhavale, V. M.; Eldho, K. M.; Kurungot, S.; Ajithkumar, T. G.; Vaidhyanathan, R. 1000-fold enhancement in proton conductivity of a MOF using post-synthetically anchored proton transporters. *Sci Rep* **2016**, *6*, Article number: 32489.

(32) Zhao, S. N.; Song, X. Z.; Zhu, M.; Meng, X.; Wu, L. L.; Song, S. Y.; Wang, C.; Zhang, H. J. Assembly of three coordination polymers based on a sulfonic-carboxylic ligand showing high proton conductivity. *Dalton Trans.* **2015**, *44*, 948-954.

(33) Nguyen, M. V.; Lo, T. H. N.; Luu, L. C.; Nguyen, H. T. T.; Tu, T. N. Enhancing proton conductivity in a metal-organic framework at T > 80 degrees C by an anchoring strategy. *J. Mater. Chem. A* **2018**, *6*, 1816-1821.

(34) Sadakiyo, M.; Yamada, T.; Kitagawa, H. Proton Conductivity Control by Ion Substitution in a Highly Proton-Conductive Metal-Organic Framework. *J. Am. Chem. Soc.* **2014**, *136*, 13166-13169.

(35) Nagarkar, S. S.; Unni, S. M.; Sharma, A.; Kurungot, S.; Ghosh, S. K. Two-in-One: Inherent Anhydrous and Water-Assisted High Proton Conduction in a 3D Metal-Organic Framework. *Angew. Chem.-Int. Edit.* **2014**, *53*, 2638-2642.

(36) Kang, D. W.; Kang, M.; Hong, C. S. Post-synthetic modification of porous materials: superprotonic conductivities and membrane applications in fuel cells. *J. Mater. Chem. A* **2020**, *8*, 7474-7494.

(37) Sumida, K.; Rogow, D. L.; Mason, J. A.; McDonald, T. M.; Bloch, E. D.; Herm, Z. R.; Bae, T. H.; Long, J. R. Carbon Dioxide Capture in Metal-Organic Frameworks. *Chem. Rev.* **2012**, *112*, 724-781.

(38) Seoane, B.; Coronas, J.; Gascon, I.; Benavides, M. E.; Karvan, O.; Caro, J.; Kapteijn, F.; Gascon, J. Metal-organic framework based mixed matrix membranes: a solution for highly efficient CO2 capture? *Chem. Soc. Rev.* **2015**, *44*, 2421-2454.

(39) Qiu, S. L.; Xue, M.; Zhu, G. S. Metal-organic framework membranes: from synthesis to separation application. *Chem. Soc. Rev.* **2014**, *43*, 6116-6140.

(40) An, J.; Rosi, N. L. Tuning MOF CO2 Adsorption Properties via Cation Exchange. *J. Am. Chem. Soc.* **2010**, *132*, 5578-+.

(41) Liao, P. Q.; Chen, H. Y.; Zhou, D. D.; Liu, S. Y.; He, C. T.; Rui, Z. B.; Ji, H. B.; Zhang, J. P.; Chen, X. M. Monodentate hydroxide as a super strong yet reversible active site for CO2 capture from high-humidity flue gas. *Energy Environ. Sci.* **2015**, *8*, 1011-1016.

(42) Duan, J. G.; Yang, Z.; Bai, J. F.; Zheng, B. S.; Li, Y. Z.; Li, S. H. Highly selective CO2 capture of an agw-type metal-organic framework with inserted amides: experimental and theoretical studies. *Chem. Commun.* **2012**, *48*, 3058-3060.

(43) Xiong, S. S.; He, Y. B.; Krishna, R.; Chen, B. L.; Wang, Z. Y. Metal-Organic Framework with Functional Amide Groups for Highly Selective Gas Separation. *Cryst. Growth Des.* **2013**, *13*, 2670-2674.

(44) Liao, P. Q.; Chen, X. W.; Liu, S. Y.; Li, X. Y.; Xu, Y. T.; Tang, M. N.; Rui, Z. B.; Ji, H. B.; Zhang, J. P.; Chen, X. M. Putting an ultrahigh concentration of amine groups into a metal-organic framework for CO2 capture at low pressures. *Chem. Sci.* **2016**, *7*, 6528-6533.

(45) Milner, P. J.; Martell, J. D.; Siegelman, R. L.; Gygi, D.; Weston, S. C.; Long, J. R. Overcoming double-step CO2 adsorption and minimizing water co-adsorption in bulky diamine-appended variants of Mg-2(dobpdc). *Chem. Sci.* **2018**, *9*, 160-174.

(46) Abedi, S.; Morsali, A. Ordered Mesoporous Metal Organic Frameworks Incorporated with Amorphous TiO2 As Photocatalyst for Selective Aerobic Oxidation in Sunlight Irradiation. *ACS Catal.* **2014**, *4*, 1398-1403.

(47) Santaclara, J. G.; Olivos-Suarez, A. I.; Gonzalez-Nelson, A.; Osadchii, D.; Nasalevich, M. A.; van der Veen, M. A.; Kapteijn, F.; Sheveleva, A. M.; Veber, S. L.; Fedin, M. V.; Murray, A. T.; Hendon, C. H.; Walsh, A.; Gascon, J. Revisiting the Incorporation of Ti(IV) in UiO-type Metal-Organic Frameworks: Metal Exchange versus Grafting and Their Implications on Photocatalysis. *Chem. Mat.* **2017**, *29*, 8963-8967.

(48) Wiers, B. M.; Foo, M. L.; Balsara, N. P.; Long, J. R. A Solid Lithium Electrolyte via Addition of Lithium Isopropoxide to a Metal-Organic Framework with Open Metal Sites. *J. Am. Chem. Soc.* **2011**, *133*, 14522-14525.

(49) Ameloot, R.; Aubrey, M.; Wiers, B. M.; Gomora-Figueroa, A. P.; Patel, S. N.; Balsara, N. P.; Long, J. R. Ionic Conductivity in the Metal-Organic Framework UiO-66 by Dehydration and Insertion of Lithium tert-Butoxide. *Chem.-Eur. J.* **2013**, *19*, 5533-5536.

(50) Chand, S.; Elahi, S. M.; Pal, A.; Das, M. C. Metal-Organic Frameworks and Other Crystalline Materials for Ultrahigh Superprotonic Conductivities of 10(-2) S cm(-1) or Higher. *Chem.-Eur. J.* **2019**, *25*, 6259-6269.

(51) Kim, S.; Joarder, B.; Hurd, J. A.; Zhang, J. F.; Dawson, K. W.; Gelfand, B. S.; Wong, N. E.; Shimizu, G. K. H. Achieving Superprotonic Conduction in Metal-Organic Frameworks through Iterative Design Advances. *J. Am. Chem. Soc.* **2018**, *140*, 1077-1082.

(52) Li, X. M.; Liu, J.; Zhao, C.; Zhou, J. L.; Zhao, L.; Li, S. L.; Lan, Y. Q. Strategic hierarchical improvement of superprotonic conductivity in a stable metal-organic framework system. *J. Mater. Chem. A* **2019**, *7*, 25165-25171.

(53) Mukhopadhyay, S.; Debgupta, J.; Singh, C.; Sarkar, R.; Basu, O.; Das, S. K. Designing UiO-66-Based Superprotonic Conductor with the Highest Metal-Organic Framework Based Proton Conductivity. *ACS Appl. Mater. Interfaces* **2019**, *11*, 13423-13432.

(54) Yang, F.; Xu, G.; Dou, Y. B.; Wang, B.; Zhang, H.; Wu, H.; Zhou, W.; Li, J. R.; Chen, B. L. A flexible metal-organic framework with a high density of sulfonic acid sites for proton conduction. *Nat. Energy* **2017**, *2*, 877-883.

(55) Vilela, S. M. F.; Firmino, A. D. G.; Mendes, R. F.; Fernandes, J. A.; Ananias, D.; Valente, A. A.; Ott, H.; Carlos, L. D.; Rocha, J.; Tome, J. P. C.; Paz, F. A. A. Lanthanide-polyphosphonate coordination polymers combining catalytic and photoluminescence properties. *Chem. Commun.* **2013**, *49*, 6400-6402.

(56) Cunha-Silva, L.; Lima, S.; Ananias, D.; Silva, P.; Mafra, L.; Carlos, L. D.; Pillinger, M.; Valente, A. A.; Paz, F. A. A.; Rocha, J. Multi-functional rare-earth hybrid layered networks: photoluminescence and catalysis studies. *J. Mater. Chem.* **2009**, *19*, 2618-2632.

(57) Cunha-Silva, L.; Mafra, L.; Ananias, D.; Carlos, L. D.; Rocha, J.; Paz, F. A. A. Photoluminescent lanthanide-organic 2D networks: A combined synchrotron powder X-ray diffraction and solid-state NMR study. *Chem. Mat.* **2007**, *19*, 3527-3538.

(58) Vilela, S. M. F.; Fernandes, J. A.; Ananias, D.; Carlos, L. D.; Rocha, J.; Tome, J. P. C.; Paz, F. A. A. Photoluminescent layered lanthanide-organic framework based on a novel trifluorotriphosphonate organic linker. *Crystengcomm* **2014**, *16*, 344-358.

(59) Silva, P.; Vieira, F.; Gomes, A. C.; Ananias, D.; Fernandes, J. A.; Bruno, S. M.; Soares, R.; Valente, A. A.; Rocha, J.; Paz, F. A. A. Thermal Transformation of a Layered Multifunctional Network into a Metal-Organic Framework Based on a Polymeric Organic Linker. *J. Am. Chem. Soc.* **2011**, *133*, 15120-15138.

(60) Vilela, S. M. F.; Ananias, D.; Gomes, A. C.; Valente, A. A.; Carlos, L. D.; Cavaleiro, J. A. S.; Rocha, J.; Tome, J. P. C.; Paz, F. A. A. Multi-functional metal-organic frameworks assembled from a tripodal organic linker. *J. Mater. Chem.* **2012**, *22*, 18354-18371.

(61) Vilela, S. M. F.; Ananias, D.; Fernandes, J. A.; Silva, P.; Gomes, A. C.; Silva, N. J. O.; Rodrigues, M. O.; Tome, J. P. C.; Valente, A. A.; Ribeiro-Claro, P.; Carlos, L. D.; Rocha, J.; Paz, F. A. A. Multifunctional micro-and nanosized metalorganic frameworks assembled from bisphosphonates and lanthanides. *J. Mater. Chem. C* **2014**, *2*, 3311-3327.

(62) Hermer, N.; Reinsch, H.; Mayer, P.; Stock, N. Synthesis and characterisation of the porous zinc phosphonate Zn-2(H2PPB)(H2O)(2) center dot xH(2)O. *Crystengcomm* **2016**, *18*, 8147-8150.

(63) Mah, R. K.; Lui, M. W.; Shimizu, G. K. H. Enhancing Order and Porosity in a Highly Robust Tin(IV) Triphosphonate Framework. *Inorg. Chem.* **2013**, *52*, 7311-7313.

(64) Ouellette, W.; Wang, G. B.; Liu, H. X.; Yee, G. T.; O'Connor, C. J.; Zubieta, J. The Hydrothermal and Structural Chemistry of Oxovanadium-Arylphosphonate Networks and Frameworks. *Inorg. Chem.* **2009**, *48*, 953-963.

(65) Pili, S.; Argent, S. P.; Morris, C. G.; Rought, P.; Garcia-Sakai, V.; Silverwood, I. P.; Easun, T. L.; Li, M.; Warren, M. R.; Murray, C. A.; Tang, C. C.; Yang, S. H.; Schroder, M. Proton Conduction in a Phosphonate-Based Metal-Organic Framework Mediated by Intrinsic "Free Diffusion inside a Sphere". *J. Am. Chem. Soc.* **2016**, *138*, 6352-6355.

(66) Taddei, M.; Costantino, F.; Vivani, R.; Sabatini, S.; Lim, S. H.; Cohen, S. M. The use of a rigid tritopic phosphonic ligand for the synthesis of a robust honeycomb-like layered zirconium phosphonate framework. *Chem. Commun.* **2014**, *50*, 5737-5740.

(67) Alexandrov, E. V.; Blatov, V. A.; Kochetkov, A. V.; Proserpio, D. M. Underlying nets in three-periodic coordination polymers: topology, taxonomy and prediction from a computer-aided analysis of the Cambridge Structural Database. *Crystengcomm* **2011**, *13*, 3947-3958.

(68) Blatov, V. A.; Shevchenko, A. P.; Serezhkin, V. N. TOPOS3.2: a new version of the program package for multipurpose crystal-chemical analysis. *Journal of Applied Crystallography* **2000**, *33*, 1193.

(69) Ma, K. R.; Wei, C. L.; Zhang, Y.; Kan, Y. H.; Cong, M. H.; Yang, X. J. Structures and Spectroscopy Studies of Two M(II)-Phosphonate Coordination Polymers Based on Alkaline Earth Metals (M = Ba, Mg). *J. Spectrosc.* **2013**, *378379*

(70) Navarro, J. A. R.; Barea, E.; Rodriguez-Dieguez, A.; Salas, J. M.; Ania, C. O.; Parra, J. B.; Masciocchi, N.; Galli, S.; Sironi, A. Guest-induced modification of a magnetically active ultramicroporous, gismondine-like, Copper(II) coordination network. *J. Am. Chem. Soc.* **2008**, *130*, 3978-3984.

(71) Procopio, E. Q.; Linares, F.; Montoro, C.; Colombo, V.; Maspero, A.; Barea, E.; Navarro, J. A. R. Cation-Exchange Porosity Tuning in Anionic Metal-Organic Frameworks for the Selective Separation of Gases and Vapors and for Catalysis. *Angew. Chem.-Int. Edit.* **2010**, *49*, 7308-7311.

(72) Lopez-Maya, E.; Montoro, C.; Colombo, V.; Barea, E.; Navarro, J. A. R. Improved CO2 Capture from Flue Gas by Basic Sites, Charge Gradients, and Missing Linker Defects on Nickel Face Cubic Centered MOFs. *Adv. Funct. Mater.* **2014**, *24*, 6130-6135.

(73) Kim, E. J.; Siegelman, R. L.; Jiang, H. Z. H.; Forse, A. C.; Lee, J. H.; Martell, J. D.; Milner, P. J.; Falkowski, J. M.; Neaton, J. B.; Reimer, J. A.; Weston, S. C.; Long, J. R. Cooperative carbon capture and steam regeneration with tetraamine-appended metal-organic frameworks. *Science* **2020**, *369*, 392-396.

(74) Franz, R. D. Comparisons of pKa and log P values of some carboxylic and phosphonic acids: Synthesis and measurement. *AAPS Pharmsci* **2001**, *3*, rticle number: 1

(75) Smit, B.; Reimer, J. R.; Oldenburg, C. M.; Bourg, I. C. *Introduction to Carbon Capture and Sequestration*; Imperial College Press, 2014.

(76) Boyd, P. G.; Chidambaram, A.; Garcia-Diez, E.; Ireland, C. P.; Daff, T. D.; Bounds, R.; Gladysiak, A.; Schouwink, P.; Moosavi, S. M.; Maroto-Valer, M. M.; Reimer, J. A.; Navarro, J. A. R.; Woo, T. K.; Garcia, S.; Stylianou, K. C.; Smit, B. Data-driven design of metal-organic frameworks for wet flue gas CO2 capture. *Nature* **2019**, *576*, 253-256.

(77) Matsuda, R.; Kitaura, R.; Kitagawa, S.; Kubota, Y.; Belosludov, R. V.; Kobayashi, T. C.; Sakamoto, H.; Chiba, T.; Takata, M.; Kawazoe, Y.; Mita, Y. Highly controlled acetylene accommodation in a metal-organic microporous material. *Nature* **2005**, *436*, 238-241.

(78) Luna-Triguero, A.; Vicent-Luna, J. M.; Madero-Castro, R. M.; Gomez-Alvarez, P.; Calero, S. Acetylene Storage and Separation Using Metal-Organic Frameworks with Open Metal Sites. *ACS Appl. Mater. Interfaces* **2019**, *11*, 31499-31507.

(79) Sarkisov, L.; Harrison, A. Computational structure characterisation tools in application to ordered and disordered porous materials. *Mol. Simul.* **2011**, *37*, 1248-1257.

(80) Afonso, R.; Sardo, M.; Mafra, L.; Gomes, J. R. B. Unravelling the Structure of Chemisorbed CO2 Species in Mesoporous Aminosilicas: A Critical Survey. *Environ. Sci. Technol.* **2019**, *53*, 2758-2767.

(81) Mafra, L.; Cendak, T.; Schneider, S.; Wiper, P. V.; Pires, J.; Gomes, J. R. B.; Pinto, M. L. Structure of Chemisorbed CO2 Species in Amine-Functionalized Mesoporous Silicas Studied by Solid-State NMR and Computer Modeling. *J. Am. Chem. Soc.* **2017**, *139*, 389-408.

(82) Li, X. M.; Dong, L. Z.; Li, S. L.; Xu, G.; Liu, J.; Zhang, F. M.; Lu, L. S.; Lan, Y. Q. Synergistic Conductivity Effect in a Proton Sources-Coupled Metal Organic Framework. *ACS Energy Lett.* **2017**, *2*, 2313-2318.

(83) Mendes, R. F.; Barbosa, P.; Domingues, E. M.; Silva, P.; Figueiredo, F.; Paz, F. A. A. Enhanced proton conductivity in a layered coordination polymer. *Chem. Sci.* **2020**, *11*, 6305-6311.

(84) Meng, X.; Wang, H. N.; Song, S. Y.; Zhang, H. J. Proton-conducting crystalline porous materials. *Chem. Soc. Rev.* **2017**, *46*, 464-480.

(85) Bao, S. S.; Shimizu, G. K. H.; Zheng, L. M. Proton conductive metal phosphonate frameworks. *Coord. Chem. Rev.* **2019**, *378*, 577-594.

Table of Contents Graphic